BAND-LIMITED CORONAGRAPHS USING A HALFTONE DOT PROCESS: DESIGN GUIDELINES, MANUFACTURING, AND LABORATORY RESULTS

P. MARTINEZ[1], C. DORRER[2], AND M. KASPER[1]
[1] European Southern Observatory, Karl-Schwarzschild-Strasse 2, D-85748, Garching, Germany
[2] Aktiwave, 241 Ashley drive, Rochester, NY, 14620, USA

ABSTRACT

The Exo-Planet Imaging Camera and Spectrograph for the future 42 m European-Extremely Large Telescope will enable direct images and spectra for both young and old Jupiter-mass planets in the infrared. To achieve the required contrast, several coronagraphic concepts—to remove starlight—are under investigation: conventional pupil apodization (CPA), apodized-pupil Lyot coronagraph (APLC), dual-zone coronagraph (DZC), four-quadrants phase mask (FQPM), multi-stages FQPM, annular groove phase mask, high-order optical vortex, and band-limited coronagraph (BLC). Recent experiment demonstrated the interest of a halftone dot process—namely microdots technique—to generate the adequate transmission profile of pupil apodizers for CPA, APLC, and DZC concepts. Here, we examine the use of this technique to produce band-limited focal plane masks, and present guidelines for the design. Additionally, we present the first near-IR laboratory results with BLCs that confirm the microdots approach as a suitable technique for ground-based observations.

Key words: instrumentation: high angular resolution – techniques: high angular resolution

Online-only material: color figures

1. INTRODUCTION

By the end of 2018, challenging projects such as Exo-Planet Imaging Camera and Spectrograph (EPICS; Kasper et al. 2008) for the future 42 m European-Extremely Large Telescope, or Planet Formation Imager (PFI; Macintosh et al. 2006b) for the Thirty Meter Telescope (TMT) will enable direct images, and spectra for warm self-luminous and reflected-light Jovian planets. These instruments will operate with eXtreme Adaptive Optics system (XAO) designed for high Strehl ratios (i.e., ∼90% in *H*-band), as for the Spectro-Polarimetric High-Contrast Exoplanet Research (SPHERE; Beuzit et al. 2008) and the Gemini Planet Imager (GPI; Macintosh et al. 2006a), forthcoming planet-finder instruments with first light planned 2011.

Several coronagraph concepts have been studied extensively in the past years, with the objective of finding optimized designs that can sufficiently suppress the on-axis starlight, allowing faint companions direct detection (e.g., Malbet 1996; Sivaramakrishnan et al. 2001; Guyon et al. 2006; Martinez et al. 2008a). Among them, the band-limited coronagraph (BLC; Kuchner & Traub 2002) has been proposed to completely remove starlight. The BLC has the advantage of being less sensitive to the primary mirror segmentation, unavoidable with ELTs, than for other concepts (Sivaramakrishnan & Yaitskova 2005), and to provide achromatic behavior. Additionally, in Martinez et al. (2008a), we pointed out the interest of such concept on an ELT for either very bright object detection, or for the search of planets at large angular separations.

Several BLC prototypes have been developed during the past years (e.g., Debes et al. 2004; Trauger et al. 2004; Crepp et al. 2006; Trauger & Traub 2007; Moody et al. 2008) for visible wavelength application. Several technical approaches have been used: (1) gray-scale pattern written with an high-energy beam sensitive glass (HEBS) using *e*-beam lithography; (2) notch filter pattern—binary mask—written with thick Chromium layer on a substrate, dry-etched with high-density-decoupled plasma; (3) a gray-scale pattern manufactured with vacuum-deposited metals and dielectrics. Even if electron-sensitized HEBS glass can accurately accommodate a continuous range of transmission, the darkening of the HEBS glass under electron bombardment is accompanied by a determined phase shift, while the technique suffers from a lack of experience in the near-IR. Same constraints apply for the vacuum-deposited metal technique. The notch filter has the advantage of being intrinsically achromatic. These designs, consisting of a particular implementation of small structures (stripes of opaque material with width of about some microns) must be finely controlled in size, spacing, and opacity. Mask errors and tolerance are discussed in Kuchner & Spergel (2003), where requirements might be strong for near-IR application.

In this paper, we examine the use of a halftone dot process, namely microdot technique, to reproduce a continuous mask profile as already done for pupil apodizer for SPHERE (Martinez et al. 2009a, 2009b), and being manufactured for the *James Webb Space Telescope* (*JWST*) NIRCam coronagraph (Krist 2009). These masks consist of distributions of opaque square pixels (called dots) to reproduce the continuous transmission of a filter with several advantages: relative ease of manufacture, achromaticity, reproducibility, and ability to generate continuous transmission ranges, without introducing wavefront errors. Besides, mask errors can be easily pre-compensated (Dorrer & Zuegel 2007).

Section 2 describes the microdot design principle and properties, while Section 3 provides guidelines for the design. Section 4 presents monochromatic, and polychromatic results obtained in laboratory in the near-IR. Finally, Section 5 concludes on the suitability of the microdots approach for producing BLCs in the context of ground-based instruments.

2. PRINCIPLE

In its general scheme, a microdots filter is an array of dots (i.e., pixels) that are either opaque or transparent. It is fabricated
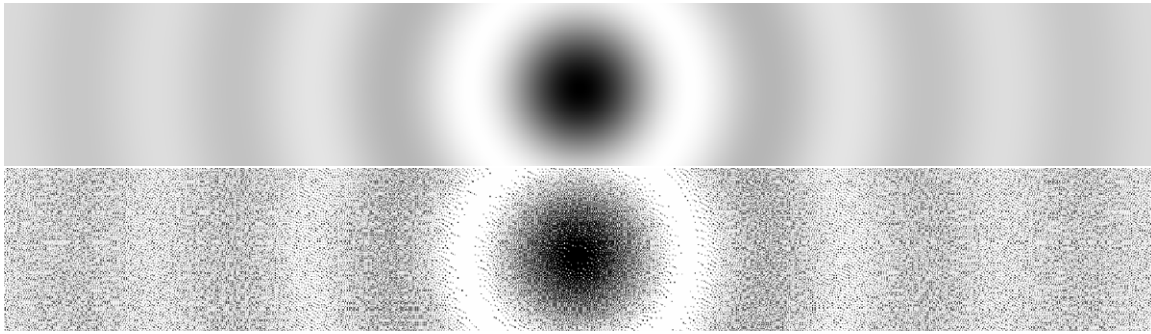
Figure 1. Simulation maps of a circular band-limited mask. Top: scan of the center (gray level pattern). Bottom: corresponding optimized microdots pattern. Gray-scale color evolves from 0% (black) to 100% (white) transmission.
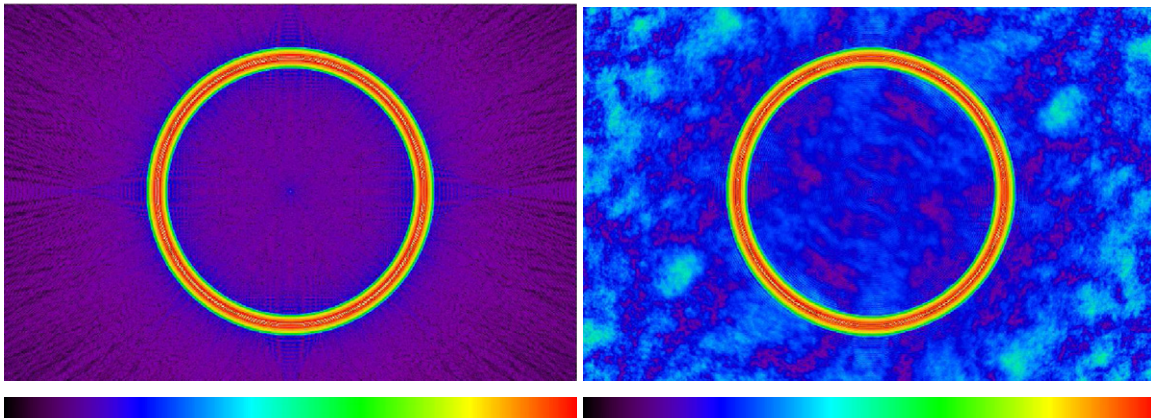

Figure 2. Example of pupil-plane images before effect of the pupil stop, with a continuous BLC (left), and a microdot BLC (right). The arbitrary false color distribution has been chosen to enhance contrast for the sake of clarity. The scale evolves from noise level (black/pink) to maximum intensity (red).

(A color version of this figure is available in the online journal.)

by lithography of a light-blocking metal layer deposited on a transparent glass substrate. To best approximate specifications, the dot distribution is regulated by a Floyd–Steinberg dithering algorithm (Floyd & Steinberg 1976), based on the error-diffusion principle. This allows the accurate generation of gray levels, and rapidly varying shaping functions. This algorithm is presented and discussed in Ulichney (1987, 1988) for printing technique applications, as well as for laser beam shaping (Dorrer & Zuegel 2007). Additionally, this algorithm was successfully used for producing microdots pupil apodizers for the apodized pupil Lyot coronagraph (Martinez et al. 2009a, 2009b).

By principle, the microdot mask—the BLC amplitude function—is sampled, subject to the dot size (see Figure 1). This issue will be further discussed in Section 3 from a design specification point of view. In the following, we will examine its impact on the coronagraphic effect by comparing to that of a continuous transmission mask.

We consider a telescope with aperture function A, and a band-limited amplitude mask function from Kuchner & Traub (2002):

$$M(r) = N \left(1 - \mathrm{sinc} \left(\frac{\epsilon r D}{\lambda} \right) \right), \qquad (1)$$

where λ is the wavelength of the application, r is the radial coordinates in the image plane, D is the telescope primary diameter, ϵ is the bandwidth which rules the inner working angle of the coronagraph (IWA hereafter), and finally N is a constant of normalization insuring that $0 \leqslant M(r) \leqslant 1$.

The Fourier transform of $M(r)$ denoted as $\mathcal{M}(u)$ is therefore

$$\mathcal{M}(u) = N \left(\delta \left(\frac{u\lambda}{D} \right) - \frac{\lambda}{\epsilon D} \times \Pi \left(\frac{u\lambda}{\epsilon D} \right) \right), \qquad (2)$$

where u states for the radial coordinate of the pupil plane, δ is the Dirac function, and Π is the top-hat function.

In a BLC, the incident electromagnetic field propagates from the telescope aperture to a focal plane where the mask, $M(r)$, is applied. After the occulting mask (filtering for the low frequencies), the pupil is re-imaged in a second pupil plane where a pupil stop is placed (high-frequency filter). Then the scientific image is recorded in a second focal plane where the detector is installed. The coronagraphic effect can be well described in the second pupil plane (ψ_{pp}, hereafter), as the convolution product of $\mathcal{M}(u)$ by the telescope aperture $A(u)$, times the pupil-stop function denoted $S(u)$, such as

$$\psi_{pp} = [\mathcal{M}(u) \star A(u)] \times S(u), \qquad (3)$$

where the star ($\star$) states for the convolution product. The power of band-limited coronagraph comes from the properties that $\mathcal{M}(u)$ is equal to zero everywhere but $|u| < \frac{\epsilon D}{2\lambda}$, i.e., the power spectrum of $M(r)$ has power in a limited domain of frequencies. As a result, in the second pupil plane (Equation (3)), the convolution product of $\mathcal{M}(u)$ by the pupil aperture confines the diffracted light in the vicinity of the pupil edges as exhibits in Figure 2(left, where the pink color states for the numerical noise level). This energy can be completely removed with the pupil stop, $S(u)$, similar to the aperture function, but reduced in the diameter. A development of the BLC
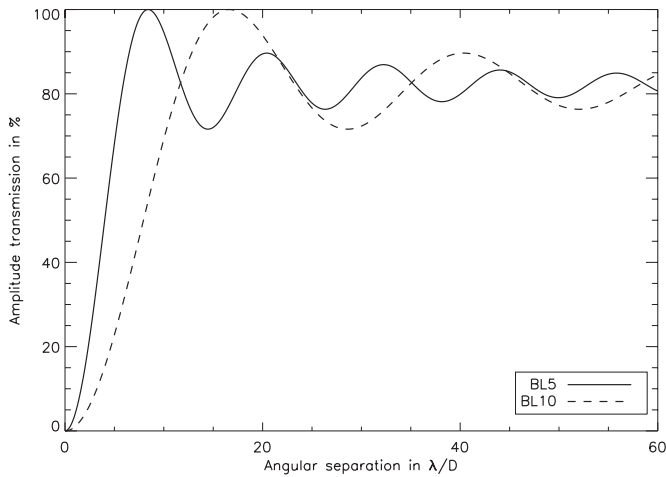
Figure 3. Band-limited functions used in simulation, and in the experiment.

theory can be found in Kuchner & Traub (2002), although we note that the present formalism assumes that the amplitude mask is purely real, i.e., it does not take into account the relationship between opacity and phase shift in real physical material, which impacts the performances.

A microdot BLC will have a different power spectrum than a continuous mask because its function is sampled by the dots, which forces its Fourier transform to be periodic, and the algorithm used to distribute dots introduce high-frequency noise. As a result, the convolution product of $\mathcal{M}(u)$ by the pupil aperture still confines the diffracted light in the vicinity of the pupil edges, but some energy remain inside and outside the geometrical pupil as exhibited in Figure 2 (right). The residual part inside the geometrical pupil, not filtered by the pupil stop, will therefore set a limit in the achievable performance. The intensity of the residual energy as seen in Figure 2 (right) is four to five order of magnitude bellow the maximum intensity of the ring surrounding the pupil aperture. The amount of residual energy in the pupil plane is a function of the dots size, and the bandwidth of the function (ϵ), since these two parameters directly impact the sampling of the design. This point will be further analyzed in Section 3.2 with simulations.

Although BLC designed with microdots cannot achieve perfect cancelation of starlight, it is important to note that a ground-based instrument does not require an ideal performance of a BLC, but can accommodate with the relaxed performance since limitation will first come from the quasi-static speckle halo level. Planet-finder instruments will use speckle calibration strategies to improve contrast delivered after the correction of the turbulence by an adaptive optic system (AO). If a simultaneous speckle rejection technique is used (e.g., simultaneous differential imaging, spectral deconvolution), as selected for SPHERE, GPI, and EPICS, performance of a coronagraph does not necessarily need to be better than this quasi-static speckle halo level (10^{-5}–10^{-6}). A deeper contrast is then achievable through appropriate data reduction.

3. MASK DESIGN GUIDELINES

3.1. Specified Functions

We consider two BLC masks with an identical function (Equation (1)), but different bandwidths (i.e., different ϵ values, see Figure 3). Hereafter, BL5 and BL10 correspond, respectively, to $\epsilon = 0.17$ (IWA = $5\lambda/D$) and $\epsilon = 0.086$ (IWA =

$10\lambda/D$). Even if BL10 has a large IWA ($\sim 0\rlap{.}{''}08$ in H-band for a 42 m telescope), only suitable to the search of companions at large angular separations, it has a smoother transition in between the low- and high-transmission parts of its profile, and can be compared with BL5 in the light of the technique employed (i.e., sampling issue).

3.2. Size of the Dots

The selection of the dots size is in first approximation–as discussed in Section 2—formally equivalent to a sampling problem. Better results are obtained with smaller pixels, since this allows a finer control of the local transmission. This is particularly an important issue in the region of the mask where transmission is very low (center of the mask). Since BLC masks are placed in the focal plane of an instrument, their dimensions are usually expressed in λ/D units. Therefore, a simple metric to quantify the sampling of the function is the ratio of the Airy unit by the dot size (p). Optimally, this metrics must be defined at the shortest wavelength for which the mask is designed to operate, and can be expressed as

$$s = \frac{F_\# \times \lambda_{\min}}{p}, \qquad (4)$$

where $F_\#$ is the f-number on the mask, and $\lambda_{\min}$ is the shortest wavelength of the application (i.e., insuring that s remains greater than the specification for all wavelengths). Using simulation maps of microdots BLC (assuming specified dot spatial distribution), we analyzed how the dot size affects the coronagraphic performance with respect to continuous idealistic masks. Our simulations make the use of Fraunhofer propagators between pupil and image planes, which is implemented as fast Fourier transforms (FFTs) generated with an IDL code. Dots are sampled by one pixels to prevent from the excessive size of array critical in the high s values domain. Validity of the dot sampling has been verified with simulations assuming different samplings (1, 4, and 16 pixels per dot), as discussed in Martinez et al. (2009a). An effect is only expected in the very low s domain at high-spatial frequencies, out of the field of view of interest. These monochromatic and aberration-free simulations were addressed for the two band-limited configurations we manufactured (BL5 and BL10). Results are presented in Figure 4. Note that a continuous mask provides a total on-axis source suppression (hence not plotted in the figure) assuming the idealistic conditions of these simulations. As expected (Section 2), the ideal performance of the BLC cannot be met (i.e., contrast deeper than 10^{-12} in Figure 4). However, several s configurations (8, 16, and 32) yield interesting contrast levels, deep enough to meet contrast requirements of planet-finder projects. Considering our application (H band, $\lambda_0 = 1.6\ \mu$m, with a contrast requirements of 10^{-6} at $5\lambda/D$ after the coronagraph, e.g., EPICS), suitable configurations are $s = 8$ and $s = 16$, as the $s = 32$ situation yields to very small dots size (2.5 μm) comparable to the size of the wavelength of light. In this particular situation, it is difficult to predict how the field will react to such grating, where scalar diffraction theory does not apply. Additionally, since ϵ impacts the gradient from the very low-transmission maintained at the center to the high-transmission part (bandwidth of the function), a better performance is obtained when ϵ is larger (Figure 4, top and bottom). The issue is that the very low transmission maintained at the center of the BLC functions is significantly impacted by the dot size. This point will be further discussed in Section 3.3.
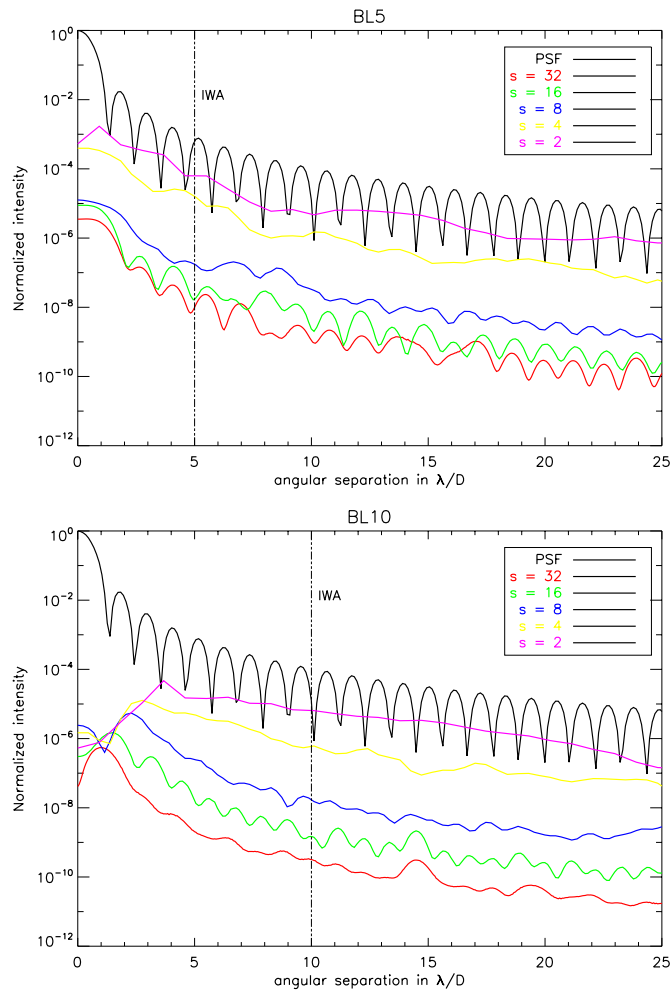
Figure 4. Impact of the dot size on the coronagraphic performance for BL5 (top) and BL10 (bottom).

(A color version of this figure is available in the online journal.)

Figure 5. Impact of the mask bandwidth on the IWA and performance.

(A color version of this figure is available in the online journal.)

such as

$$OD(e, \lambda) = \frac{4\pi k(\lambda)e}{\lambda \times \ln(10)}, \qquad (5)$$

where k describes the linear attenuation of the optical wave (material-dependent), e stands for the propagation distance (i.e., the material thickness), and λ is the operating wavelength. Equation (5) is further detailed in the Appendix. The OD must be therefore carefully defined, accordingly with the expected performance of the coronagraph (s and ϵ-dependent, Figures 4 and 5).

4. EXPERIMENT

4.1. Optical Setup

The optical setup is a near-IR coronagraphic transmission bench developed at ESO (Figure 6). All the optics are set on a table with air suspension in a dark room and are fully covered with protection panels forming a nearly closed box. The entrance aperture is fulfilled, and has a 3 mm diameter (Φ) made in a laser-cut, stainless-steel sheet to an accuracy of 0.002 mm. BLC masks were installed at an F/48.4 beam. Reimaging optics were made with IR achromatic doublets. The pupil stop has a diameter $D_{\mathrm{stop}} = 0.84 \times \Phi$, and remains the same during the experiment. Its optimization gave emphasis to the achromatic behavior of BLCs. The quality of the collimation in pupil planes was checked and adjusted using an HASO 64 Shack–Hartmann sensor. A pupil-imager system was implemented to align the pupil-stop mask with the entrance-pupil mask to complete alignment in the x- and y-directions. The coronagraphic focal plane was localized using a visible CCD mini-camera with a HeNe laser light and tuned in the final IR image on the detector. The IR camera used (the Infrared Test Camera) uses a HAWAII $1k \times 1k$ detector, cooled to $103°$ K with a vacuum pressure of 10^{-5} mbar. Internal optics were designed to reach a pixel scale of 5.3 mas (almost 8 pixels per λ/D). Experiment was done in H band using either a narrow filter ($\Delta\lambda/\lambda = 1.4\%$), or a broadband filter ($\Delta\lambda/\lambda = 24\%$). The Strehl ratio of the bench was evaluated to ~92%. It was determined by measuring the peaks intensity ratio of the experimental point-spread function (PSF) to that of the theoretical PSF normalized to the total intensity. The theoretical PSF is created through two different methods, both converging to the same Strehl ratio: (1) by performing the

3.3. Function Bandwidth

The bandwidth parameter of BL functions (ϵ) directly impacts the gradient from the low to the high-transmission part of the profile and rules the IWA of the coronagraph; it is, therefore, important to analyze its effect on the performance. We simulated several cases with different ϵ values (from 0.095 to 0.8, i.e., IWA from 1 to 9 λ/D; see Figure 5) for the $s = 16$ cases. Results gathered in Figure 5 show that for the IWA larger than $3\lambda/D$ ($\epsilon < 0.28$) performance in the halo is not ϵ-dependent, while only a slight difference is observable on the peak. For the IWA between 3 and $2\lambda/D$, although an important degradation of performance appears, coronagraphic capabilities are not negligible (contrast of 10^{-5} at the IWA). Under $2\lambda/D$ IWA, the situation degrades further.

3.4. Dot Opacity

Whatever the regime of wavelength for which the device is designed, the optical density (OD) is a critical issue to avoid leaks of the starlight at the center of the detector image. The OD is guaranteed by sufficient thickness of the metal layer (denoted e hereafter). For visible application, Chrome layers are commonly used, while for near-IR applications, more opaque materials are mandatory (Aluminum, for instance). The OD is defined at a specific wavelength, and for a given material, and thickness
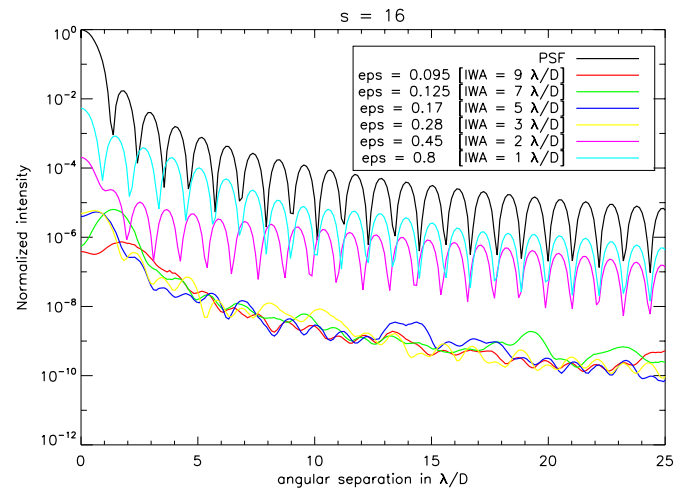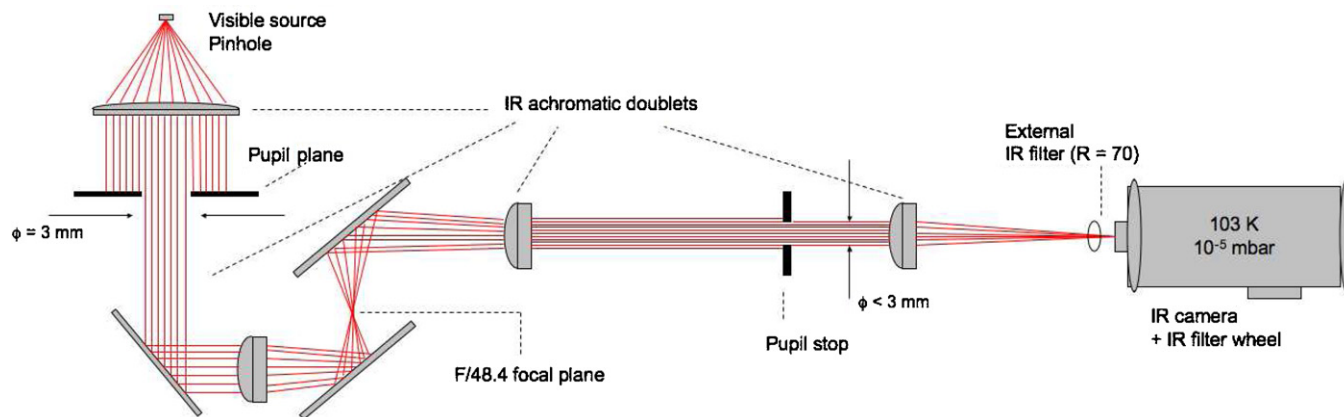
Figure 6. Schematic setup of the coronagraphic test-bench.
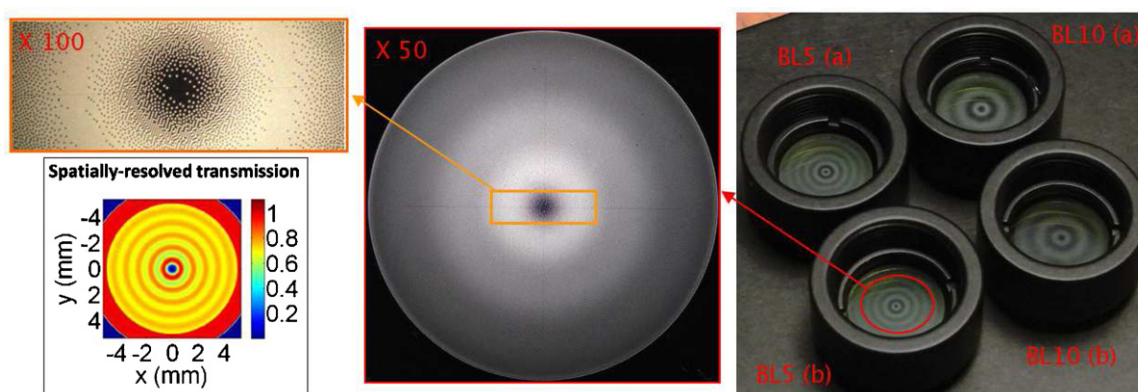(A color version of this figure is available in the online journal.)

Figure 7. Four prototypes manufactured as seen in their integration mounts (right), successive Shadowgraph inspections (middle and top-left, $\times$ 50 and $\times$ 100), as well as a spatially resolved transmission of BL5 (b) recorded at 1.0 microns (bottom-left).
(A color version of this figure is available in the online journal.)

forward FFT of the autocorrelation of an oversampled and uniformly illuminated entrance pupil image from our telescope pupil mask; (2) by performing the FFT of a simulated aperture function with the radius determined from the experimental PSF on the basis of photometric criteria.

4.2. Prototypes

Four prototypes were manufactured by Precision Optical imaging (Rochester, New-York), two BL5, and two BL10 masks. All the masks were designed for 1.64 μm (*H* band), and fabricated using wet-etch contact lithography of an aluminum layer (OD = 8+, e = 2000 Å) deposited on a BK7 substrate (λ/10 peak-to-valley, 0''5 diameter). Antireflection coating has been applied for each faces ($R < 0.5\%$ from 1.2 to 1.8 μm). For each design (BL5 and BL10), two dot sizes have been produced: 5 and 10 μm (i.e., s = 16 and 8) denoted by (a) and (b), respectively (see Figure 7). The OD has been specified to guarantee against leakage greater than the intrinsic limitation of the microdot technique (for s = 16 and 8, see Figure 4). All the masks have been inspected and cleaned up before integration (Figure 7). Profiles were measured at 1.0 μm. The spatially resolved transmission has been obtained after background subtraction and flat field normalization. Profile accuracy is of about 5% of the specification. The error is mostly localized in the outer part of the mask (high-transmission part), while the center part (for the low transmissions) is highly accurate (Figure 8). The error in the outer part took its origin in a

calibration issue of the process, which will be corrected for with new prototypes.

4.3. Results

The following metrics are used to evaluate coronagraphic abilities to suppress the on-axis starlight.

1. τ stands for the *total rejection rate*: the ratio of total intensity of the direct image to that of the coronagraphic image.
2. τ_0 stands for the *peak attenuation rate*: the ratio of the maximum of the direct image to that of the coronagraphic image.
3. $\mathscr{C}$ stands for the *contrast*: the ratio of the coronagraphic image at a given angular separation to that of the maximum of the direct image to the intensity, azimuthally averaged.

4.3.1. Data Acquisition and Reduction

To achieve high-dynamic range measurements, a series of 3 s short exposure images averaged over 3 minutes, and the presence or absence of neutral density filters, were employed. Neutral density filters were only applied on non-coronagraphic images. PSFs and coronagraphic images were dark subtracted by turning off the light. The data-reduction process is corrected for bad pixels, background, and scales images by the exposure time and optical density.
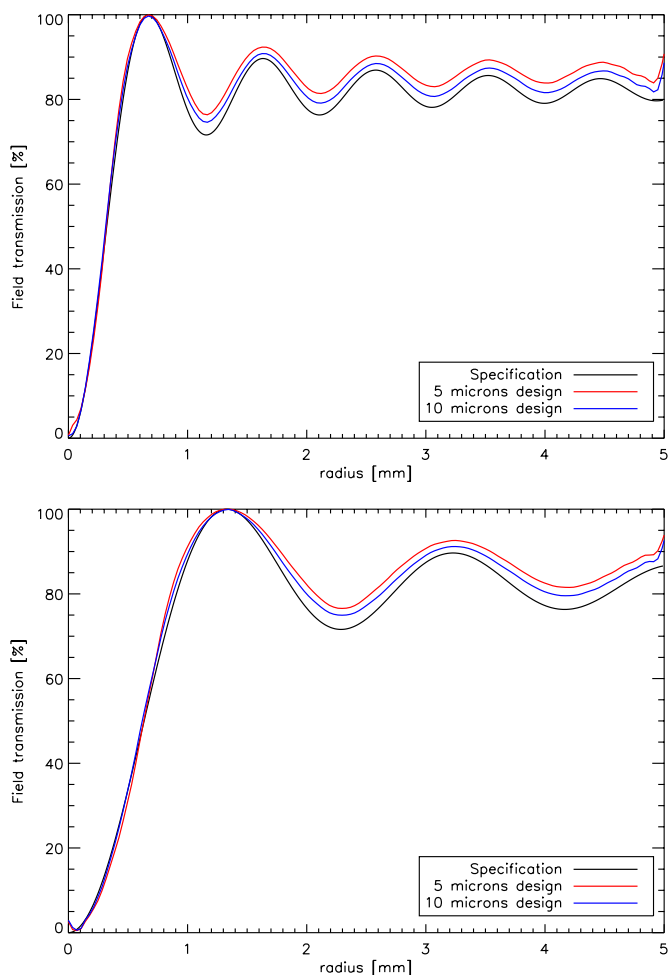
Figure 8. Measured profiles of BL5 (top), BL10 (bottom), and specification for the two dot-size prototypes (5 μm and 10 μm).

(A color version of this figure is available in the online journal.)

4.3.2. Results with BL5

BL5 prototypes have been tested with the narrow ($\Delta\lambda/\lambda$ = 1.4%) and broadband ($\Delta\lambda/\lambda$ = 24%) filters. Coronagraphic images are presented in Figure 9, while profiles of BL5(a) and BL5(b) are gathered in Figure 10 (top). All coronagraphic runs made with BL5(a) and BL5(b), whatever the filter, roughly yield to the identical performance. BL5 demonstrates an achromatic

behavior as expected for such coronagraph. No difference between BL5(a) and BL5(b) has been observed; therefore, regarding to the performance obtained, $s = 16$ and 8 are suitable configurations. A discrepancy of ~1 order of magnitude for both BL5(a) and BL5(b) has been revealed on the peak, while in the halo it evolves between two and three orders of magnitude (see theoretical results as a function of s in Figure 4, left). Despite this discrepancy, these first results (gathered in Table 1) are better than the SPHERE prototypes performance (Boccaletti et al. 2008), and experimental results reached on the same bench with an APLC (Martinez et al. 2009a). However, we note that these prototypes (Four Quadrant Phase Mask, and APLC) were tuned for a very small IWA (1, and 2.3 λ/D, respectively, compared to 5 and 10 for the BLC described here). Contrast evolves from ~3×10^{-5} at the IWA to ~3×10^{-8} at 20λ/D (cut-off frequency of the SPHERE-like AO system).

4.3.3. Results with BL10

Results presented with BL10 prototypes (Figure 10, bottom) correspond to $\Delta\lambda/\lambda$ = 24%. As for BL5, we did not notice any difference between performance reached either by BL10(a) or BL10(b). Contrast evolves from ~1×10^{-7} at IWA to ~1×10^{-8} at 20λ/D, while the peak attenuation rate is about 10^5. A discrepancy of about one order of magnitude has been revealed on the peak as for BL5, while in the halo it evolves between one and two orders of magnitude at the IWA, and at 25λ/D depending on which configuration of BL10 we are looking at (Figure 4, left). As expected, BL10 results went beyond BL5 performance, although the IWA is quite large. The coronagraphic image exhibits speckle halo (Figure 9) induced by the non-perfect nature of optics used in the bench. This point is further discussed in Section 4.4.2.

4.4. Performance Limitations

The discrepancy revealed in the experiment may find its origin in several error sources, among them—for the most important ones—the scatter light due to imperfect optical components that create speckles in the scientific image, and mask profile errors. Note that the source diameter ($0.082\lambda/D$) and the alignment errors of the masks are negligible considering the IWA of the BLCs, while the impact of the filter bandpass is not considered because of the achromatic behavior of BLCs (confirmed in the experiment). We also neglect the fact that the pupil stop is not black-coated (e.g., black anodization) which may produce potential reflections.
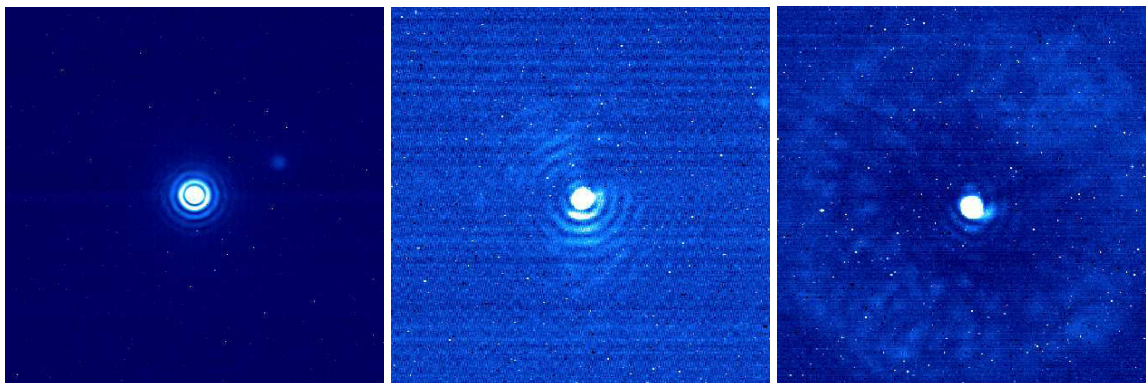

Figure 9. From left to right: PSF image (with a ghost, right side of the image), BL5 coronagraphic image, and BL10 coronagraphic image ($\Delta\lambda/\lambda$ = 24%). The image dynamic has been chosen to enhance contrast for the sake of clarity.

(A color version of this figure is available in the online journal.)

Table 1
Summary of Coronagraphic Results Obtained with BL5 and BL10 ($\Delta\lambda/\lambda = 24\%$)

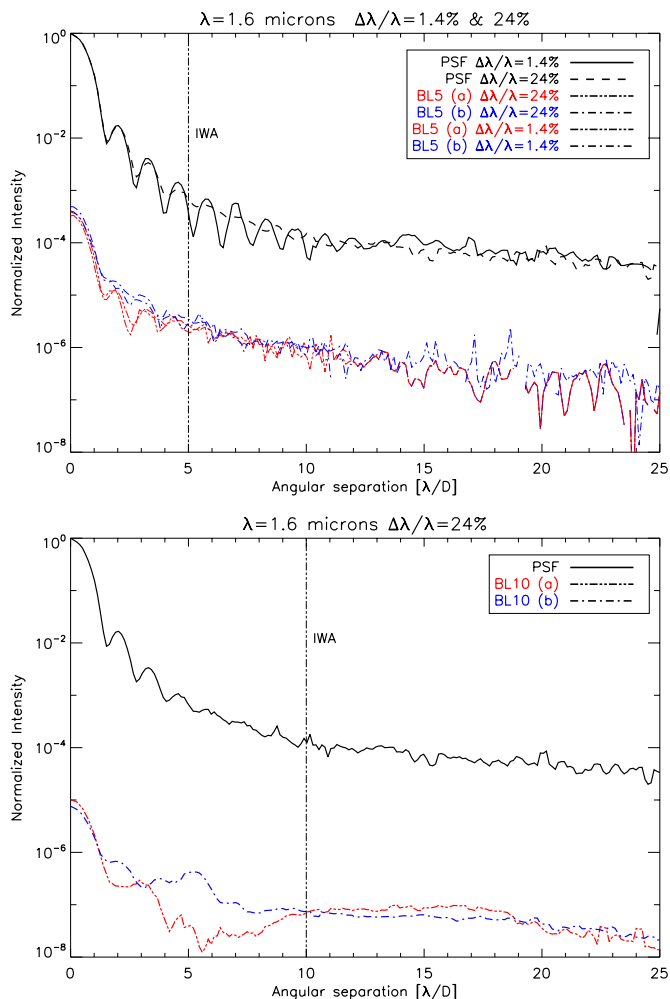| Metrics	τ	τ_0	$\mathscr{C}_{\text{IWA}}$	$\mathscr{C}_{12\lambda/D}$	$\mathscr{C}_{20\lambda/D}$	$\mathscr{C}_{25\lambda/D}$
BL5 (a)	2410	2554	3.7×10^{-5}	5.6×10^{-7}	2.7×10^{-8}	5.3×10^{-8}
BL5 (b)	1804	2038	3.0×10^{-5}	8.1×10^{-7}	2.6×10^{-7}	8.5×10^{-8}
BL10 (a)	81606	97375	1.5×10^{-7}	7.7×10^{-8}	3.7×10^{-8}	1.3×10^{-8}
BL10 (b)	83177	131809	1.3×10^{-7}	6.3×10^{-8}	4.3×10^{-8}	2.1×10^{-8}

Figure 10. Experimental results obtained with BL5 (top) and BL10 (bottom) prototypes, all profiles are azimuthally averaged.
(A color version of this figure is available in the online journal.)

4.4.1. Mask Profile Errors

Simulations using real measured profiles (i.e., global profile measured after free-space propagation of the BLC masks and using an imaging optical system, Figure 8 for instance) showed that profile errors are actually responsible of one order of magnitude loss on the peak while the halo is less affected. Assuming their respective measured profile errors, the rejection factor for BL5 and BL10 ($s = 16$) is, respectively, limited to $\tau_{\text{mask}} = 6400$ and 108000.

Ideally, going to very small pixel size improves the accuracy of the mask profile transmission (i.e., the sampling problem). In practice, two constraints set a limit on the interest of a very small pixel size: (1) getting good accuracy becomes more difficult because fabrication errors become more important as the pixel size decreases; (2) when the pixel size is comparable

to the wavelength of light, the transmission is affected by plasmons (Genet & Ebbesen 2007; Huang & Zhu 2007). In such situation, the transmission might be strongly dependent on the wavelength. Therefore, it is very likely that efforts must be focused on reducing fabrication errors to avoid an increase of transmission, as a result of a reduction of the metal dots during the isotropic wet-ech lithography process. An improvement of the pre-compensation algorithm applied on the digital design correcting for edge effects on the light-blocking metal dots by estimating the feature size that would be obtained after fabrication is thus critical.

4.4.2. Wavefront Errors

The wavefront error (wavefront high-frequency components) of the optical components prior to the pupil stop imposes an important limitation when reaching high contrast. The optical components on the bench upstream of the pupil stop have a standard quality: flats mirrors of $\lambda/10$ ptv (i.e., $\lambda/35$ rms), and achromatic doublets of $\lambda/5$ rms, over the full diameter (25.4 mm) at 633 nm, which corresponds, respectively, to $\sim\lambda/300$ and $\sim\lambda/45$ rms for the 3 mm pupil diameter (assuming the quality scales linearly with the beam size). Taking into account all components, and assuming that phase added quadratically, it corresponds to an overall approximated total amount of wavefront error of $\sim\lambda/67$ rms at 1.6 μm, (i.e., 24 nm rms). With simulations using a Fraunhofer propagator IDL code, and assuming theoretical mask profile, and using typical power law of manufactured optics, described by PSDs with f^{-2} variation (Duparré et al. 2002), where f is the spatial frequency, we actually found that 12 nm rms prior to the pupil stop, already imposes a contrast floor between 10^{-7} and 10^{-8}, which is in good agreement with the wavefront error estimation discussed above, which is commonly used as a rule of thumb for order of magnitude estimation, as performed in Riaud et al. (2003). For 12 nm rms, the total rejection factor for BL5 and BL10 ($s = 16$) is, respectively, limited to: $\tau_{\text{wavefront}} = 40400$, and 188200.

4.4.3. Performance Estimation versus Experimental Results

Assuming that these independent errors are added quadratically, the global rejection factor of BLs including mask error, and wavefront errors is

$$\tau = \frac{1}{\sqrt{\left(\frac{1}{\tau_{\text{mask}}^2} + \frac{1}{\tau_{\text{wavefront}}^2}\right)}}, \quad (6)$$

which correspond to $\tau_{\text{BL5}} = 6300$ and $\tau_{\text{BL10}} = 93600$. These estimations are in agreement with experimental results (Table 1). Note that τ refers to a global performance estimation (integrated metric of the overall images; see Section 4.3), and can therefore not inform for a local coronagraphic profile behavior. Figure 11 gathers experimental and theoretical results for BL10 ($s = 16$) with a broadband filter ($\Delta\lambda/\lambda = 24\%$), with simulated profiles obtained assuming an independently mask profile error and a
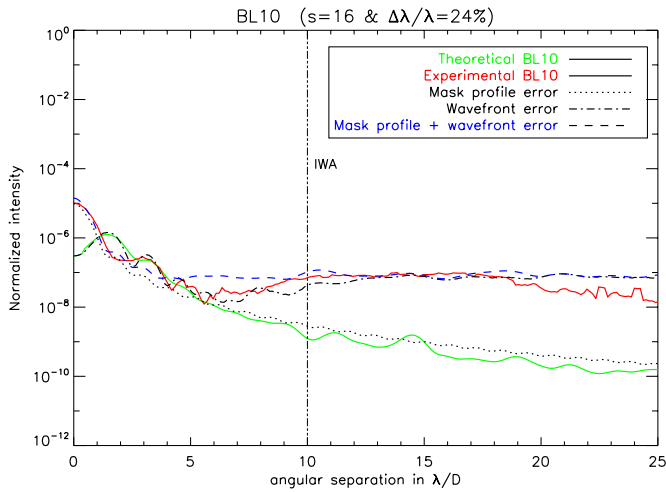
Figure 11. Resume of BL10 ($s = 16$ and $\Delta\lambda/\lambda = 24\%$) theoretical (green curve) and experimental results (red curve) compared to simulation profiles obtained, when including error sources such as mask profile error (dotted black curve), wavefront error (12 nm rms, fullfilled black curve), or both of these errors (blue curve).

(A color version of this figure is available in the online journal.)

wavefront error (12 nm rms), as well as a profile including both of these error sources in the same time. Even if it is difficult to ascertain source of errors, the profile error is consistent with the discrepancy found at small angular separation (i.e., peak level error), while the wavefront errors are probably the dominant source of the error in the halo. In that situation, the intrinsic limitation of the microdots technique is therefore not a limiting factor.

5. CONCLUSION

We have described the development and laboratory experiment of band-limited coronagraphs using a microdots design in the near-IR. In this paper, we provide design guidelines and demonstrate the microdots technique as a promising solution for BLC for ground-based observations.

We have shown with numerical simulations that although total starlight cancelation is not possible, theoretical contrast offers with the microdot approach are deep enough to guarantee that the BLC will not set a limit on the performance of a ground-based instrument. We note that the theoretical treatment presented in this study does not consider the complexity introduced by potential spectral, and polarization effects of the physical mask.

We identified two sampling configurations suitable for near-IR experiment: $s = 16$ and 8, yielding to an identical performance in the experiment. Additionally, we pointed out that the interest of the microdots technique in the light of contrast and IWA requirements is not dependent on the function bandwidth (ϵ) assuming IWA $\geqslant 3\lambda/D$. This already meets EPICS (20–30 mas in H band), or SPHERE (0.″1 in H band) standard requirements. However, we note that stronger requirements of the IWA (1 or 2 λ/D, ultimate goal of SPHERE) will set a limit on the interest of the technique.

With prototypes we have demonstrated the impressive performance where limitations have been presumably (on the basis of simulations) introduced either by a mask error, or wavefront error of the bench. Improvement of the results presented and resumed in Table 1 are foreseen—at least for the peak attenuation—with a new set of prototypes that will provide a

better accuracy of the profile in the outer part of the function (the calibration issue of the manufacturing process).

Additionally, these raw polychromatic results presented belong as the first tests of the BLC in the near-IR, and were managed without an active wavefront correction, nor particular data-reduction post-processing. Performance reached in the experiment went beyond to the SPHERE prototype performances, APLC results obtained so far with a microdot apodizer on the same bench, and yield to similar contrast than the ones presented in Crepp et al. (2006)—using fourth-order notch-filter mask in a monochromatic visible wavelength domain—although the IWA is not exactly identical.

Ultimately, these final prototypes will be implemented on the high-order testbench (the HOT, the AO-facility at ESO; Aller Carpentier et al. 2008), and being compared with others (FQPM, APLC, and Lyots; Martinez et al. 2008b, 2009a) with the atmospheric turbulence generator and AO correction, as already initiated with intensive simulations (Martinez et al. 2008a). Results of this experiment will be presented in a forthcoming paper.

Although this study was carried out in the context of R&D activities for EPICS, it is potentially applicable to upcoming instruments such as SPHERE or GPI. We note that the interest of the technique presented in the paper for space-based operations is subject to science cases (IWA and contrast requirements). For instance, high star–planet contrast (10^{-10} in the visible) at less than 0.″1 (Terrestrial planet) will very likely require a wavefront stability only reachable with a space telescope. In this situation, the technique employed here will impose a limit on the accessible contrast. Notch-filter masks might be more appropriate.

APPENDIX

OPTICAL DENSITY OF A SURFACE LAYER

A lossy dispersive medium can be described for optical propagation by a complex index $n + \iota k$, where n and k are related to the linear susceptibility. The index n describes the evolution of the phase of the optical wave, and k describes the linear attenuation of the optical wave. The propagation of an electromagnetic wave of wavelength $\lambda = 2\pi c$ is described by a complex wave vector $\frac{\omega}{c}(n(\lambda) + \iota k(\lambda))$, where both the index and attenuation are wavelength dependent.

The input and output electric fields after a propagation distance (e) are related by

$$E_{\text{out}} = E_{\text{in}} \times \exp\left(\iota \frac{2\pi}{\lambda}(n(\lambda) + \iota k(\lambda)e\right). \qquad \text{(A1)}$$

The intensity transmission ($T = E_{out}/E_{in}$) for a thickness e and wavelength (λ) is therefore

$$T = \exp\left(-\frac{4\pi k(\lambda)e}{\lambda}\right). \tag{A2}$$

The optical density is by definition the base-10 logarithm of the inverse of the intensity transmission, i.e., the natural logarithm of the intensity transmission divided by the natural logarithm of 10:

$$OD(e, \lambda) = \frac{4\pi k(\lambda)e}{\lambda \ln(10)}, \tag{A3}$$

and is therefore dependent on the layer thickness (e), the operating wavelength (λ), and the factor k (material dependent).

REFERENCES

Aller Carpentier, E., et al. 2008, Proc. SPIE, 7015, 70153Z
Beuzit, J.-L., et al. 2008, Proc. SPIE, 7014, 701418
Boccaletti, A., et al. 2008, Proc. SPIE, 7015, 70156E
Crepp, J. R., Ge, J., Vanden Heuvel, A. D., Miller, S. P., & Kuchner, M. J. 2006, ApJ, 646, 1252
Debes, J. H., Ge, J., Kuchner, M. J., & Rogosky, M. 2004, ApJ, 608, 1095
Dorrer, C., & Zuegel, J. D. 2007, J. Opt. Soc. Am. B, 24, 1268
Duparré, A., et al. 2002, Appl. Opt., 41, 154
Floyd, R. W., & Steinberg, L. 1976, J. Soc. Inf. Disp. 17, 7577
Genet, C., & Ebbesen, T. W. 2007, Nature, 445, 39
Guyon, O., Pluzhnik, E. A., Kuchner, M. J., Collins, B., & Ridgway, S. T. 2006, ApJS, 167, 81
Huang, C.-P., & Zhu, Y.-Y. 2007, Active and Passive Electronic Components (New York: Hindawi Publishing Corporation)
Kasper, M., et al. 2008, Proc. SPIE, 7015, 701515
Krist, J. 2009, Proc. SPIE, 7440, 74400W
Kuchner, M. J., & Spergel, D. N. 2003, ApJ, 594, 617
Kuchner, M. J., & Traub, W. A. 2002, ApJ, 570, 900
Macintosh, B., et al. 2006a, Proc. SPIE, 6272, 62720L
Macintosh, B., et al. 2006b, Proc. SPIE, 6272, 62720N
Malbet, F. 1996, A&AS, 115, 161
Martinez, P., et al. 2008a, A&A, 492, 289
Martinez, P., et al. 2009a, A&A, 495, 363
Martinez, P., Dorrer, C., Kasper, M., & Boccaletti, A. Dohlen. 2009b, A&A, 500, 1281
Martinez, P., et al. 2008b, Proc. SPIE, 7015, 70156B
Moody, D. C., Gordon, B. L., & Trauger, J. T. 2008, Proc. SPIE, 7010, 70103P
Riaud, P., Boccaletti, A., Baudrand, J., & Rouan, D. 2003, PASP, 115, 712
Sivaramakrishnan, A., Koresko, C. D., Makidon, R. B., Berkefeld, T., & Kuchner, M. J. 2001, ApJ, 552, 397
Sivaramakrishnan, A., & Yaitskova, N. 2005, ApJ, 626, L65
Trauger, J. T., et al. 2004, Proc. SPIE, 5487, 1330
Trauger, J. T., & Traub, W. A. 2007, Nature, 446, 771
Ulichney, R. 1987, Digital Halftoning (Cambridge, MA: MIT Press)
Ulichney, R. 1988, Proc. IEEE, 76, 56